Chemical routes to materials

CrossMark

Fabrication of plate-on-plate Z-scheme SnS$_2$/Bi$_2$MoO$_6$ heterojunction photocatalysts with enhanced photocatalytic activity

Haijin Liu[1],*, Cuiwei Du[1], Haokun Bai[2], Yuzhao Su[1], Dandan Wei[1], Yuqian Wang[1], Guoguang Liu[3],*, and Lin Yang[1],*

[1] School of Environment, Henan Normal University, Key Laboratory for Yellow River and Huaihe River Water Environment and Pollution Control, Ministry of Education, Henan Key Laboratory for Environmental Pollution Control, Xinxiang 453007, People's Republic of China
[2] Faculty of Chemical, Environmental and Biological Science and Technology, Dalian University of Technology, Dalian 116024, People's Republic of China
[3] Faculty of Environmental Science and Engineering, Guangdong University of Technology, Guangzhou 510006, People's Republic of China

ABSTRACT

A class of direct plate-on-plate Z-scheme heterojunction SnS$_2$/Bi$_2$MoO$_6$ photocatalysts was synthesized via a two-step hydrothermal method. The materials were characterized by X-ray diffraction, scanning electron microscopy, transmission electron microscopy, X-ray photoelectron spectra, Fourier transform infrared photoluminescence emission spectra, and UV–vis diffuse reflectance spectroscopy. The photocatalytic activity was estimated via the degradation of crystal violet (CV) and ciprofloxacin (CIP). The experimental results indicated that the 5 wt% SnS$_2$/Bi$_2$MoO$_6$ composites exhibited significantly enhanced performance in contrast to pure Bi$_2$MoO$_6$ or SnS$_2$ nanoflakes, and were also superior to the popular TiO$_2$ (P25). The degradation reaction accorded well with the first-order reaction kinetics equation; the rate constant of CV using a SnS$_2$ content of 5 wt% photocatalyst was ∼ 3.6 times that of the Bi$_2$MoO$_6$ and 2.4 times that of SnS$_2$. Furthermore, a SnS$_2$ content of 5 wt% exhibited a 1.7 times higher photocatalytic activity of CIP than that of pure Bi$_2$MoO$_6$, and 1.3 times that of pure SnS$_2$. Radical trapping experiments and an electron spin resonance technique indicated that h$^+$ and ·OH were the dominant active species involved in the degradation process. A plasmonic Z-scheme photocatalytic mechanism was proposed to explain the superior photocatalytic activities and efficient separation of photogenerated electrons and holes.

Address correspondence to E-mail: 031163@htu.edu.cn; liugg@gdut.edu.cn; yanglin1819@163.com

🦋 Springer

Introduction

Photocatalytic technologies, as promising strategies for environmental control, have broad and attractive prospects for the degradation of water and air resident pollutants [1–4]. Over the last few decades, since water splitting on TiO_2 electrodes was initially reported, there has been an intensive focus on semiconductor-based photocatalysis [5]. As one of the most common and comprehensive photocatalytic materials, TiO_2 has typically been employed for environmentally benign water and air purification [6]. However, due to its wide band gap, the application of TiO_2 is quite limited since it can only respond to ultraviolet light, and its utilization of sunlight is poor. Furthermore, the recombination rate of electron–hole pairs is high [7]. Similarly, most single photocatalysts possess the same defects; thus, investigations into visible light-responsive photocatalysts have become intense.

Over the last few years, Bi-based materials, which are regarded as one of the most promising photocatalysts, have attracted extensive attention from researchers worldwide due to their distinguishing visible light absorption and eco-friendly characteristics. Most Bi-based photocatalysts, for example Bi_2O_3 [8], BiOX (X = Cl, Br, I) [9], $BiVO_4$ [10], $BiPO_4$ [11], $BiFeO_3$ [12], and Bi_2MoO_6 [13], are typical members of the Aurivillius oxide family. Among them, Bi_2MoO_6 is regarded as a suitable heterostructured photocatalyst candidate; it has a narrow band gap in the range of from 2.5 to 2.8 eV, and as such, it may efficiently utilize visible light. Within its phase structure, $[Bi_2O_2]^{2+}$ layers are interleaved with layers of perovskite $[MoO_4]$. Regrettably, the photocatalytic efficiency of pure Bi_2MoO_6 is poor due to the high recombination rate of photogenerated electron–hole pairs, as well as poor quantum yields and the low number of active sites, etc. [14]. Many pristine photocatalysts have similar problems. To overcome these intrinsic issues, different strategies and approaches have been undertaken, including metal and non-metal doping, morphological control, surface modification, or heterojunction formation, and more [15–17]. For example, Dutta et al. [18] reported the improved visible light photocatalytic activity of metal ion (Ti^{4+}, Mn^{2+}, Cu^{2+}, and Zn^{2+}) doped Bi_2MoO_6 for the degradation of methylene blue (MB) and malachite green (MG) dye solutions. Concurrently, novel fluorinated Bi_2MoO_6 nanocrystals for the efficient photocatalytic removal of organic pollutants in water were reported by Yu et al. [19], whereas Sun et al. successfully modified Bi_2MoO_6 nanomaterials for use as a gas sensor [20]. The most common techniques for the formation of different classes of heterojunction photocatalysts involve the introduction of foreign semiconductors, such as Z-scheme $g\text{-}C_3N_4/Bi_2MoO_6$ [20], microflower-like Fe_2O_3/Bi_2MoO_6 [21], 3D hierarchical rGO/Bi_2MoO_6 [22], sesame biscuit-like $Bi_2O_2CO_3/Bi_2MoO_6$ [23], plate-on-plate $Bi_2MoO_6/BiOCl$ [24], and more.

Currently, metal sulfides have gained in popularity due to their non-toxicity and simplicity, albeit particularly for their narrow band gaps [25–29]. The semiconductor material SnS_2 contains CdI_2-type hexagon layers with distinguishing high surface areas. In addition, it is considered as a relatively stable metal sulfide, and its band gap has been investigated to be $\sim$ 2.18–2.44 eV [25, 27]. However, the disadvantage of this material pertains to the high recombination rate of its photoexcited carriers. Presently, most SnS_2 materials are employed for Cr (VI) removal, and only in a few studies have they been used as photocatalysts. For instance, Z-scheme SnS_2/Ag_3PO_4 heterojunction photocatalysts, and $g\text{-}C_3N_4/SnS_2$ photocatalyst have been reported [30, 31]. Therefore, SnS_2-based photocatalysts are promising for further improvement and perfection.

Z-scheme photocatalysts are currently under intensive study for pollutant degradation owing to their strong redox abilities. In this study, plate-on-plate Z-scheme SnS_2/Bi_2MoO_6 heterojunction nanomaterials were synthesized by a mild hydrothermal method, and SnS_2 was grown in situ on Bi_2MoO_6 for the first time, which might facilitate intimate interfacial contacts. The photocatalytic activities of these materials were evaluated through the degradation of CV (crystal violet) and CIP (ciprofloxacin), which possess stable chemical structures, intense carcinogenicity, as well as being recalcitrant to degradation. The results indicated that the as-prepared SnS_2/Bi_2MoO_6 composites exhibited enhanced photocatalytic activities, in contrast to pure SnS_2 and Bi_2MoO_6. The highest photocatalytic efficiency of the composites was obtained by optimizing the quantity of SnS_2. Finally, the active species generated during the photocatalytic processes were detected, and a possible photocatalytic mechanism was proposed.

Experimental section

Chemicals

All chemicals were of analytical grade and used without modification. Bismuth nitrate pentahydrate $(Bi(NO_3)_3 \cdot 5H_2O, 99\%)$ was purchased from Sinopharm Chemical Reagent Co., Ltd, China. Ammonium molybdate tetrahydrate $((NH_4)_6Mo_7O_{24} \cdot 4H_2O, 99\%)$, Stannic chloride pentahydrate $(SnCl_4 \cdot 5H_2O)$, sulfourea (H_2NCSNH_2), ammonium hydroxide $(NH_3 \cdot 3H_2O)$, and ethylene glycol (EG) were purchased from Tianjin Chemical Reagent Co., Ltd., China.

Preparation of SnS_2

SnS_2 nanoflakes were synthesized using a mild hydrothermal method. The specific process was as follows: 2.1 g Stannic chloride pentahydrate and 3.0 g thiourea were initially dissolved in 70 mL distilled water, with the assistance of ultrasonication for 20 min. Subsequently, the solution was transferred into a 100-mL Teflon-lined stainless steel autoclave and heated at 180 °C for 10 h. Once the autoclave was cooled to room temperature, the yellow powder was collected, and rinsed several times with distilled water and ethanol. Finally, the precipitate was dried at 60 °C overnight.

Preparation of SnS_2/Bi_2MoO_6 composites

The SnS_2/Bi_2MoO_6 composites were synthesized via a simple hydrothermal method. In a typical synthesis, 2.25 g of $Bi(NO_3)_3 \cdot 5H_2O$ was initially dissolved in 35 mL of a 2.0 mol L^{-1} HNO_3 solution, and magnetically stirred until completely dissolved. Subsequently, 0.41 g of $(NH_4)_6Mo_7O_{24} \cdot 4H_2O$ was added, whereupon the pH value of the solution was adjusted to 7.0 using a $NH_3 \cdot 3H_2O$ solution under continued stirring for 30 min. Various quantities of SnS_2 (the weight ratios of SnS_2 to Bi_2MoO_6 were 1, 3, 5, and 7 wt%, respectively) were dispersed into ethanol (30 mL) under ultrasonication for 30 min., after which the suspension was added dropwise into the solution above. The pH value of the mixture was adjusted to 7 and stirred continuously for 30 min. Next, the solution was transferred into a 100-mL Teflon-lined stainless steel autoclave, and heated at 160 °C for 6 h, followed by cooling to room temperature. The obtained materials were filtered, rinsed with distilled water and ethanol, and dried at 60 °C in ambient air. For comparison, pure Bi_2MoO_6 was synthesized under the identical experimental conditions without the addition of SnS_2.

Characterization

The phase structure of the samples was characterized with a X–ray powder diffractometer (XRD) using a Bruker-D8-AXS diffractometer system, carried out with a Cu K_α radiation source ($\lambda = 1.5418$ nm). The morphologies and compositions of the samples were characterized via scanning electron microscopy (SEM, JEOL JSM-6390LV system). The surface states and structures of the materials were observed by high-resolution transmission emission microscopy (HRTEM, JEOL, JEM 2100) from a Japanese electronics company. The spatial elemental distribution of nanocompounds was investigated by EDS (a component of the SEM instrument). Chemical states and atomic surface elements were measured with a XSAM-800 X-ray photoelectron spectrophotometer (XPS). All binding energies were calibrated by taking the C $1s$ peak as a reference at 284.6 eV of contaminant carbon. Infrared absorption spectra were recorded using a Fourier transform infrared spectrometer (FTIR) in the frequency range of from 400 to 4000 cm^{-1}, using KBr as the reference. UV–vis diffuse reflectance spectra (DRS) were carried out with a UV–vis spectrophotometer (Lambd 950) using $BaSO_4$ as a reflectance standard. Photoluminescence (PL) spectra were collected using a florescence spectrophotometer (Cary Eclipse, Varian, USA) with a xenon lamp as an excitation source at an excitation wavelength of 340 nm. Brunauer–Emmett–Teller (BET) surface areas of the obtained samples were evaluated on the basis of nitrogen adsorption isotherms using a Micromeritics ASAP 2020 apparatus (USA). The electron spin resonance (ESR) signals of free radical species were carried out via a DMPO spin-trapping ESR technique.

Evaluation of photocatalytic activity

The photocatalytic activities of the as-prepared catalysts were evaluated through the degradation of CV (50 mL, 20 mg L^{-1}) and CIP (50 mL, 10 mg L^{-1}) in aqueous media. The photocatalytic degradation experiments were carried out in a PCX50B

multichannel catalytic reaction system with a 5 W LED light. In this PCX50B system, the quartz reaction bottles were positioned above 5 W LED white lights ($\lambda > 390$ nm). Furthermore, the controller was at the bottom of the photoreactor, which could adjust the light intensity and the speed of magnetic stirring. Nine parallel experiments can be operated simultaneously with this system, and there is no light exposure difference among the bottles. In our experiments, the suspensions were magnetically stirred for 40 min. in darkness to establish adsorption–desorption equilibrium. Subsequently, the mixtures were exposed to LED light irradiation. At regular intervals of 20 min., 3 mL of the suspensions were extracted, centrifuged, and analyzed using a UV-2900 spectrometer at wavelength of 582 nm and 276 nm for CV or CIP, respectively. The degradation efficacy during the photocatalytic process was calculated as follows:

$$\eta = \frac{C_0 - C_t}{C_0} \times 100\%$$

where C_0 is the absorbance of the original CV or CIP solution following adsorption, and C_t is the absorbance of the CV or CIP solution following light irradiation.

Results and discussion

XRD analysis

The XRD patterns of the pure as-synthesized SnS_2, Bi_2MoO_6, and SnS_2/Bi_2MoO_6 composites are shown in Fig. 1. The primary peaks in the XRD pattern of
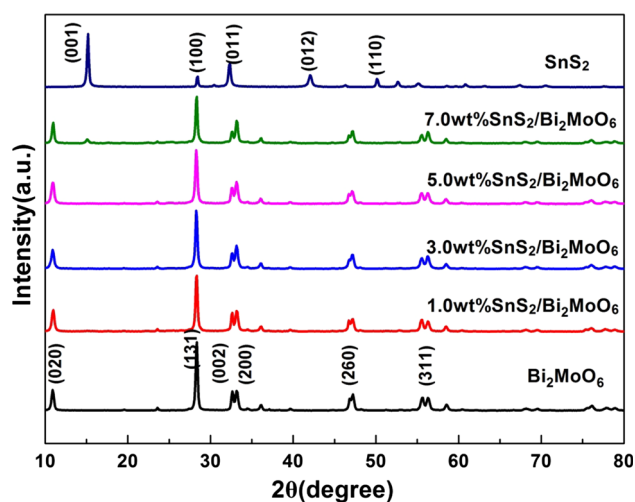

Figure 1 XRD patterns of the as-prepared samples.

SnS_2/Bi_2MoO_6 composite were consistent with those of pure Bi_2MoO_6 (JGPDS No.71-2086). The observed apparent peaks for pure Bi_2MoO_6 at 28.3°, 32.6°, 47.2°, and 55.6° corresponded with (131), (200), (260), and (331) crystal planes, respectively. For pure SnS_2, the strong diffraction peaks at $2\theta = 15.1°$, 28.3°, 32.2°, 42.0°, and 50.1° were in good agreement with (001), (100), (011), (012), and (110) diffraction planes of the hexagonal phase SnS_2 (JGPDS card No. 83-1705). The diffraction peak located at a 2θ value of 15.1° was detected in 7 wt% SnS_2/Bi_2MoO_6 composites, which was indexed to the peak of phase SnS_2, indicating that the SnS_2 was successfully introduced into the composites. Furthermore, the peak intensities at 32.6° increased along with the incrementally higher SnS_2 content, signifying that the existence of SnS_2 in the SnS_2/Bi_2MoO_6 heterojunction had some influence on the crystal structure of the Bi_2MoO_6.

SEM, TEM, and BET analysis

The morphology, microstructure, and crystalline nature of the SnS_2, Bi_2MoO_6, and SnS_2/Bi_2MoO_6 were investigated by SEM, TEM, and electron dispersive spectroscopy (EDS). It may be clearly seen from Fig. 2a that the pure SnS_2 nanoplates exhibited a hexagonal morphology with rough surfaces, which had diameters of from 400 to 600 nm. Figure 2b shows that pure Bi_2MoO_6 was composed of relatively smooth irregular nanoplates that were 1.5 μm long × 150 nm thick. The morphology of the SnS_2/Bi_2MoO_6 composite was similar to that of pure Bi_2MoO_6 with a plate-on-plate-like structure, which may be seen in Fig. 2c. The structure of SnS_2/Bi_2MoO_6 was further elucidated by EDS mapping, shown in Fig. 2d–i. The elements Bi, Mo, O, Sn, and S all existed in the 5 wt% SnS_2/Bi_2MoO_6 composite photocatalyst.

The TEM images and energy-dispersive X-ray spectroscopy (EDS) of the 5 wt% SnS_2/Bi_2MoO_6 are presented in Fig. 3. It may be clearly seen (Fig. 3a) that a SnS_2 plate grew vertically onto the surface of the Bi_2MoO_6, where the side view of the SnS_2 plate presented a regular polygon structure. The HRTEM image (Fig. 3b) provided a clearer observation of these two components. Two different sets of lattice images and their interfaces may be observed, where the lattice spacing of 0.223 and 0.27 nm corresponded to the (132) and (200) crystal planes of the Bi_2MoO_6, respectively. Further, the lattice fringe of 0.315 nm was consistent with the (100) crystal facet of the SnS_2.
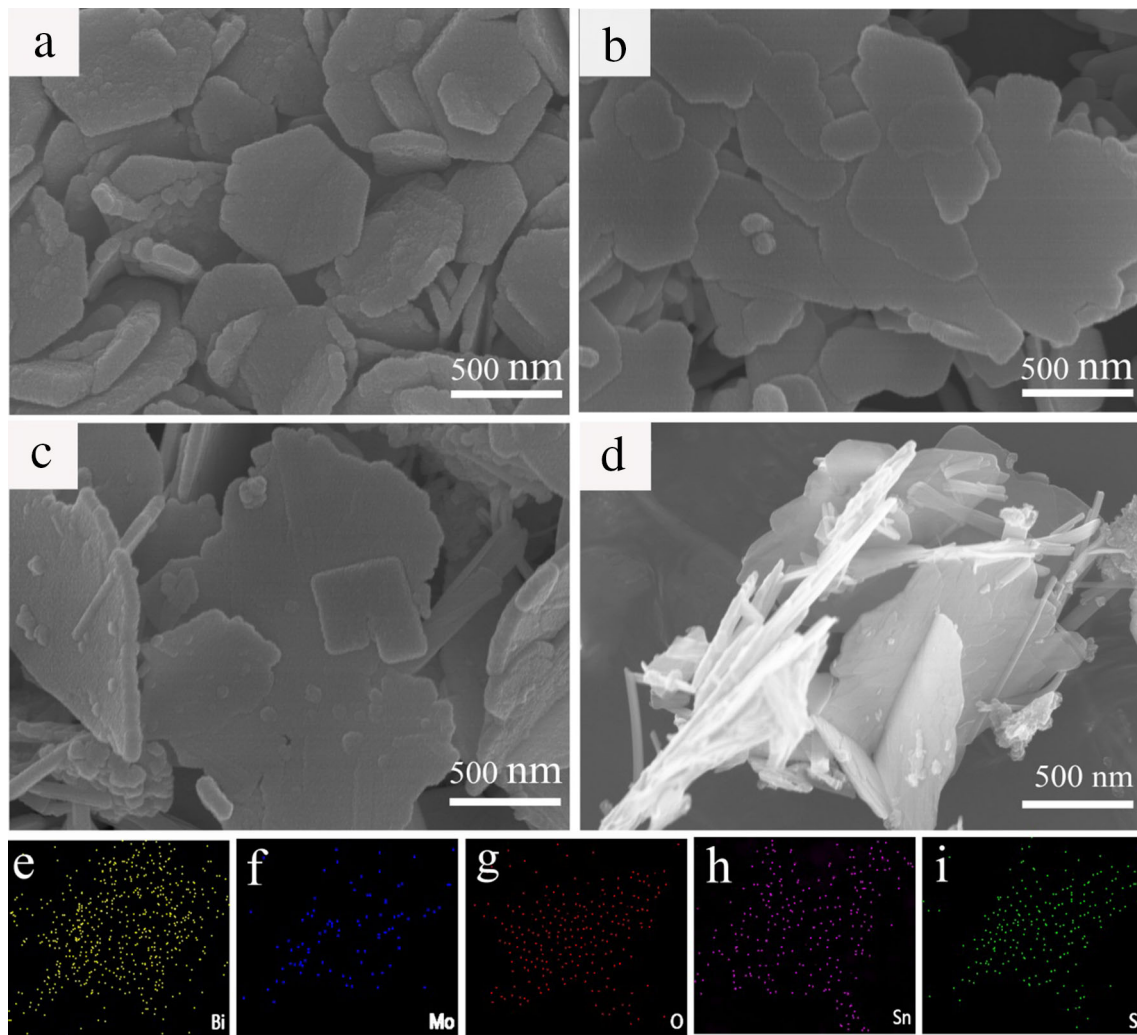
Figure 2 SEM images of pure SnS_2 (**a**), pure Bi_2MoO_6 (**b**) and 5 wt% SnS_2/Bi_2MoO_6 composites under different magnification (**c**) and (**d**).
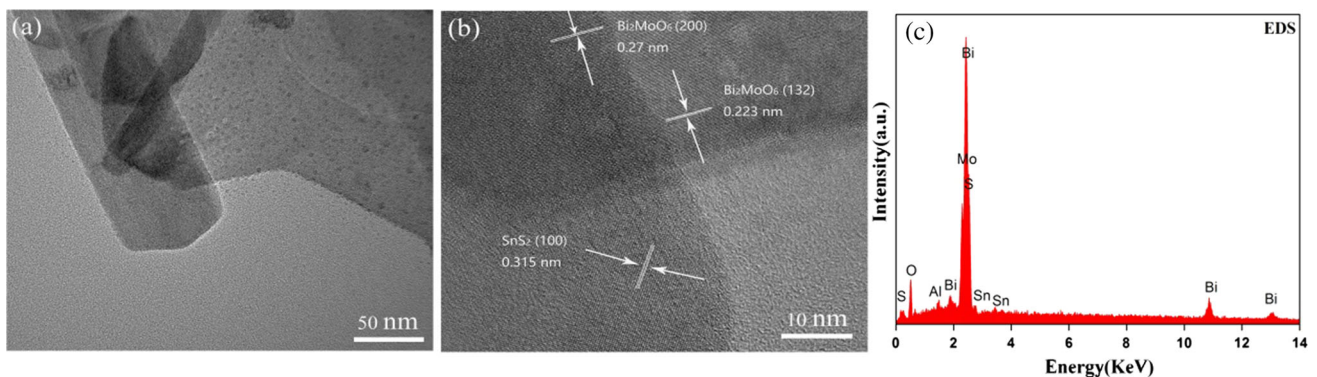
Figure 3 a Low resolution TEM image of 5 wt% SnS_2/Bi_2MoO_6; **b** High-resolution TEM image of 5 wt% SnS_2/Bi_2MoO_6; **c** EDS spectrum of 5 wt% SnS_2/Bi_2MoO_6.

Energy-dispersive spectroscopy (EDS) mapping images are displayed in Fig. 3c, where it can be observed that the Bi, Mo, O, Sn, and S elements were distributed across the surface of the SnS_2/Bi_2MoO_6 composites. Al was also present and was derived from the sample substrate.

The BET surface areas of the samples are presented in Table 1. It is revealed that the surface areas and pore volumes of SnS_2, Bi_2MoO_6, or SnS_2/Bi_2MoO_6 composites did not change significantly, indicating that the photocatalytic activities of SnS_2/Bi_2MoO_6 composites could not be improved by enlarging the surface areas. The nitrogen adsorption–desorption isotherms and pore diameter distribution of the 5% SnS_2/Bi_2MoO_6 may be found in the supporting information. The pore diameters of the samples were typically under 10 nm.

XPS analysis

The chemical elements and surface composition of the pure Bi_2MoO_6 and 5 wt% SnS_2/Bi_2MoO_6 composites are analyzed by XPS, with the results displayed in Fig. 4. The general survey scan of the 5 wt% SnS_2/Bi_2MoO_6 is presented in Fig. 4a, which shows that the surface of the composite was composed of elemental Bi, Mo, O, Sn, S, and C. The C 1s peak arose from adventitious carbon in the spectrum [32]. High-resolution X-ray photoelectron spectra are depicted in Fig. 4b–e. In Fig. 4b, the binding energies of Bi $4f_{7/2}$ and Bi $4f_{5/2}$ at 158.83 and 164.13 eV were assigned to the Bi^{3+} in Bi_2MoO_6. Subsequent to SnS_2 loading, the two peaks shifted slightly to lower energy positions at 158.43 and 163.93 eV, respectively, indicating that strong interactions might have existed between the SnS_2 and Bi_2MoO_6 [33]. Analogously, the peak positions of Mo $3d_{5/2}$ (232.03 eV) and Mo $3d_{3/2}$ (235.08 eV) in the SnS_2/Bi_2MoO_6 were lower than those of pure Bi_2MoO_6, which were located at 232.13 (Mo $3d_{5/2}$) and 235.43 eV (Mo $3d_{3/2}$) (Fig. 4c). The Sn and S elements were also detected in the SnS_2/Bi_2MoO_6 composite, with the results shown in Fig. 4d–e. It may be seen that the peaks of Sn $3d_{5/2}$ and Sn $3d_{3/2}$ existed at 486.63 and 495.28 eV, corresponding to Sn^{4+} in SnS_2. Additionally, the S 2s peaks possessed binding energies of

225.05 eV, which was attributed to the S^{2-} state. The high-resolution spectra of O are presented in Fig. 4f, which could be fitted into three peaks positioned at 529.2, 529.8, and 530.5 eV, respectively. The three peaks represented Bi–O, Mo–O, and surface hydroxyl groups (O–H) in the hybrids, respectively [20].

FTIR analysis

The FTIR spectra of the SnS_2, Bi_2MoO_6, and their composites are displayed in Fig. 5. Three characteristic band groups were observed for the Bi_2MoO_6. The absorption peaks appearing at 1636 and 3443 cm^{-1} were attributed to O–H vibrations [34]. A series of peaks from 400 to 900 cm^{-1} were attributed to Bi–O, Mo–O stretching, and Mo–O–Mo vibration modes [35]. As for the SnS_2, a broad absorption peak at 545 cm^{-1} was regarded as the vibration band of Sn–S [36]. The SnS_2 absorption peaks could not be observed in the FTIR spectrum of the composites, due to the strong stretching vibration (400–900 cm^{-1}) in the SnS_2/Bi_2MoO_6 composites.

PL analysis

The photoluminescence (PL) technique, a direct procedure for measuring band gap energies, has been widely employed for the detection and separation of photoinduced electrons and holes [37]. The PL spectra for SnS_2, Bi_2MoO_6, as well as composites, are shown in Fig. 6. The pristine SnS_2 and Bi_2MoO_6 exhibited strong emission peaks at from 450 to 550 nm, which could be ascribed to the recombination of electron–hole pairs, or through donor–acceptor recombination. Compared to pure SnS_2 and Bi_2MoO_6, the PL peak intensities were obviously decreased in the SnS_2/Bi_2MoO_6 samples, where 5 wt% SnS_2/Bi_2MoO_6 exhibited the lowest PL intensity, which indicated that the addition of SnS_2 into

Table 1 BET surface areas and pore volumes

Sample	BET surface area[a] (m^2/g)	Pore volume[b] (cm^3/g)
Bi_2MoO_6	13.6620	0.071110
SnS_2	16.1786	0.131112
1% wt% SnS_2/Bi_2MoO_6	15.4478	0.158919
3% wt% SnS_2/Bi_2MoO_6	16.2542	0.163512
5% wt% SnS_2/Bi_2MoO_6	17.4745	0.171818
7% wt% SnS_2/Bi_2MoO_6	16.5781	0.169725

[a] BET surface area is calculated basing on the linear part (P/P$_0$ = 0.3)
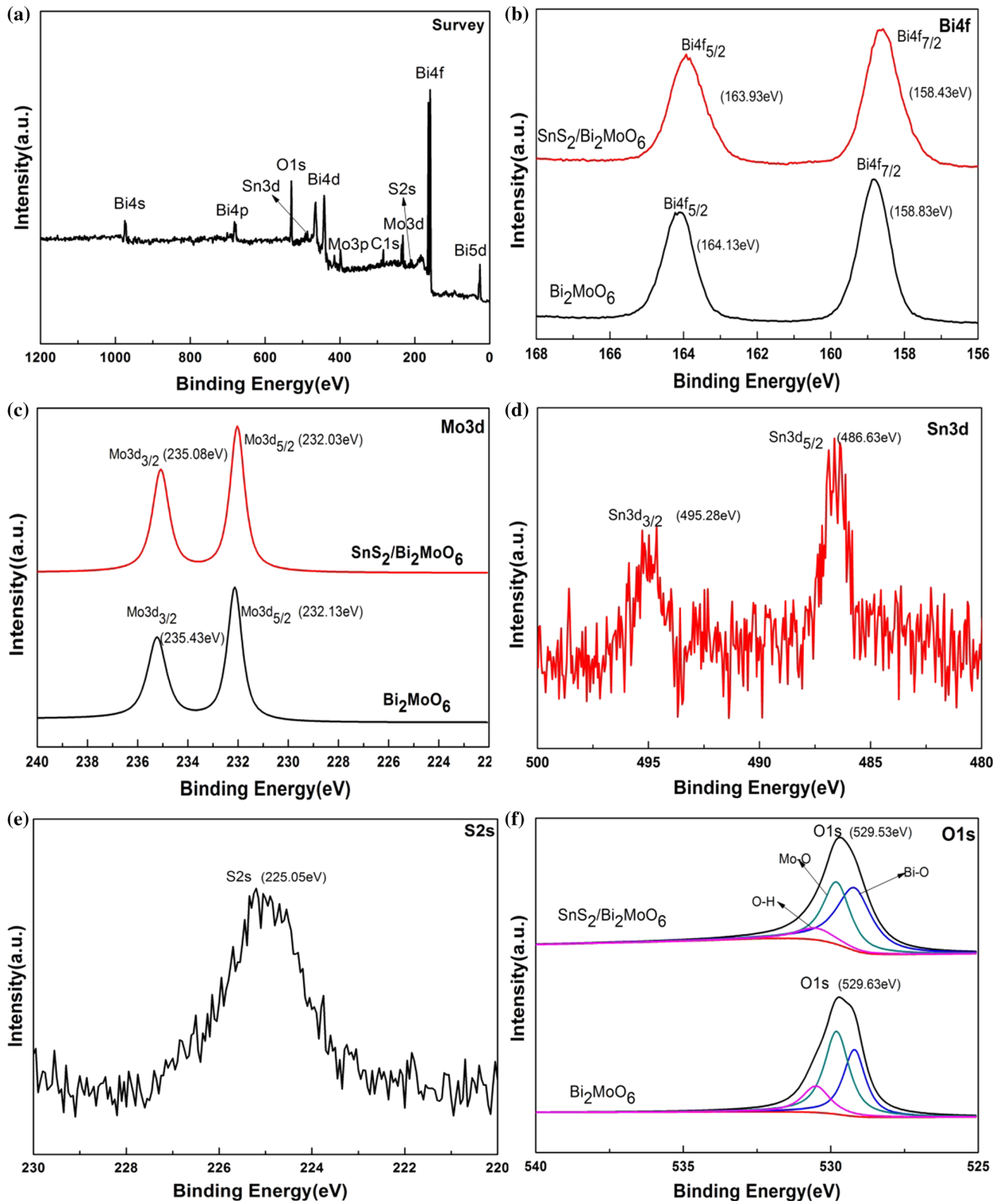
[b] Pore volume is N$_2$ adsorption volume at P/P$_0$ = 0.995

Figure 4 XPS spectra of the pure Bi_2MoO_6 and 5 wt% SnS_2/Bi_2MoO_6 composite. Survey scan of 5 wt% SnS_2/Bi_2MoO_6 (**a**). High-resolution spectra of Bi 4f (**b**), Mo 3d (**c**), Sn 3d (**d**), S 2p (**e**) and O1s (**f**).
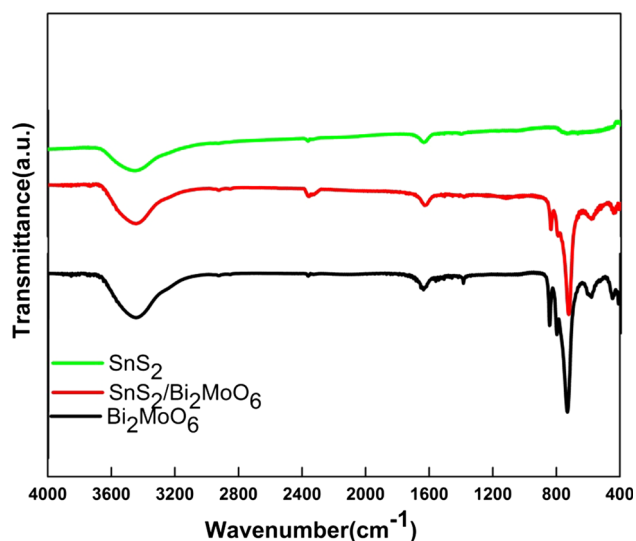
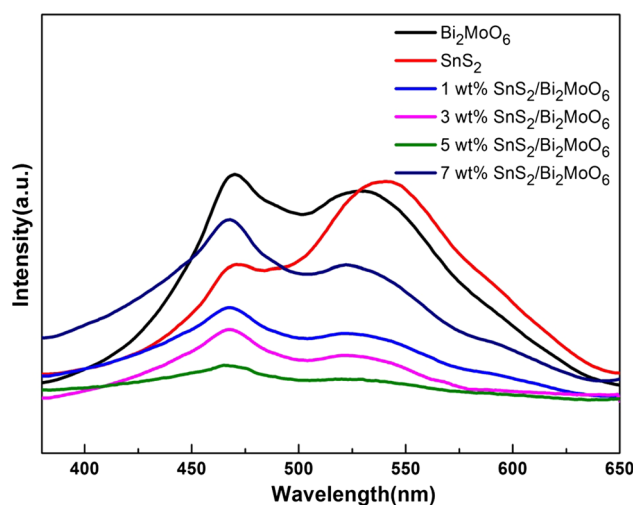**Figure 5** FTIR spectra of Bi_2MoO_6, SnS_2, and 5 wt% SnS_2/Bi_2MoO_6.

Figure 6 The photoluminescence (PL) spectra of Bi_2MoO_6, SnS_2, and SnS_2/Bi_2MoO_6.

Bi_2MoO_6 assisted with inhibiting the recombination of electron–hole pairs, which was beneficial for improving photocatalytic activity.

Photocatalytic performance of the samples

The photocatalytic activities of the prepared samples (shown in Fig. 7) were evaluated via the degradation of CV under 5 W LED light irradiation. Figure 7a–b and Table 2 display the degradation curves and rate constants. The adsorption–desorption equilibrium was established prior to the light being switched on by mixing the as-prepared photocatalysts with a CV

solution for 40 min. in the dark. The degradation of CV was negligible when there was no catalyst added, which signified that the CV molecules possessed good light stability. The photocatalytic efficiencies of the composites on the degradation of CV were significantly improved in contrast to the physical composites and pure Bi_2MoO_6 or SnS_2, and TiO_2 (P25) degraded only about 20% of CV within 120 min. The highest activity was observed for the 5 wt% SnS_2/Bi_2MoO_6 composite, where the CV was degraded to $\sim$ 82% within 120 min., which was close to twice that of pure Bi_2MoO_6, and 1.5 times that of pure SnS_2. This improvement in the photocatalytic activity might have been attributed to the formation of heterojunctions between the SnS_2 and Bi_2MoO_6. However, a higher SnS_2 content did not necessarily imply enhanced photocatalytic activity (e.g., 7 wt% SnS_2/Bi_2MoO_6 exhibited a lower photocatalytic efficiency than did the 5 wt% SnS_2/Bi_2MoO_6), which was likely due to the formation of recombination centers of photoinduced carriers by the extra SnS_2.

To quantitatively compare the photocatalytic activities of these samples, the degradation data were analyzed using a pseudo-first-order kinetic model (shown in Fig. 7b) with the formula: $\ln(C_0/C) = kt$, where k is the kinetics constant. Obviously, the largest k value of all was 1.50×10^{-2} cm^{-1} that belonged to the 5 wt% SnS_2/Bi_2MoO_6 composite, which was approximately 3.7 times that of the Bi_2MoO_6, and 2.3 times that of the SnS_2.

To test the recyclability, reuse, and stability of the 5 wt% SnS_2/Bi_2MoO_6 composite, CV degradation cycling experiments were carried out under identical conditions, with the results presented in Fig. 7c, which shows that the SnS_2/Bi_2MoO_6 composite exhibited excellent activity and stability following four consecutive runs. Subsequent to the four recycling tests, the composition of the heterojunction was examined by XRD, XPS, and FTIR. The results are depicted in Fig. 7d–f, which revealed that no obvious changes were observed in the characteristic lines during the photocatalytic processes, which indicated the very good stability of the heterojunction catalysts.

Ciprofloxacin (CIP) is a third-generation fluoroquinolone (FQ) antibiotic that is present in the ambient environment, which cannot be easily degraded during wastewater treatment. Thus, it is widely employed as a model pollutant to evaluate photocatalytic efficiency [38]. In our studies, CIP degradation was carried out over pure Bi_2MoO_6,
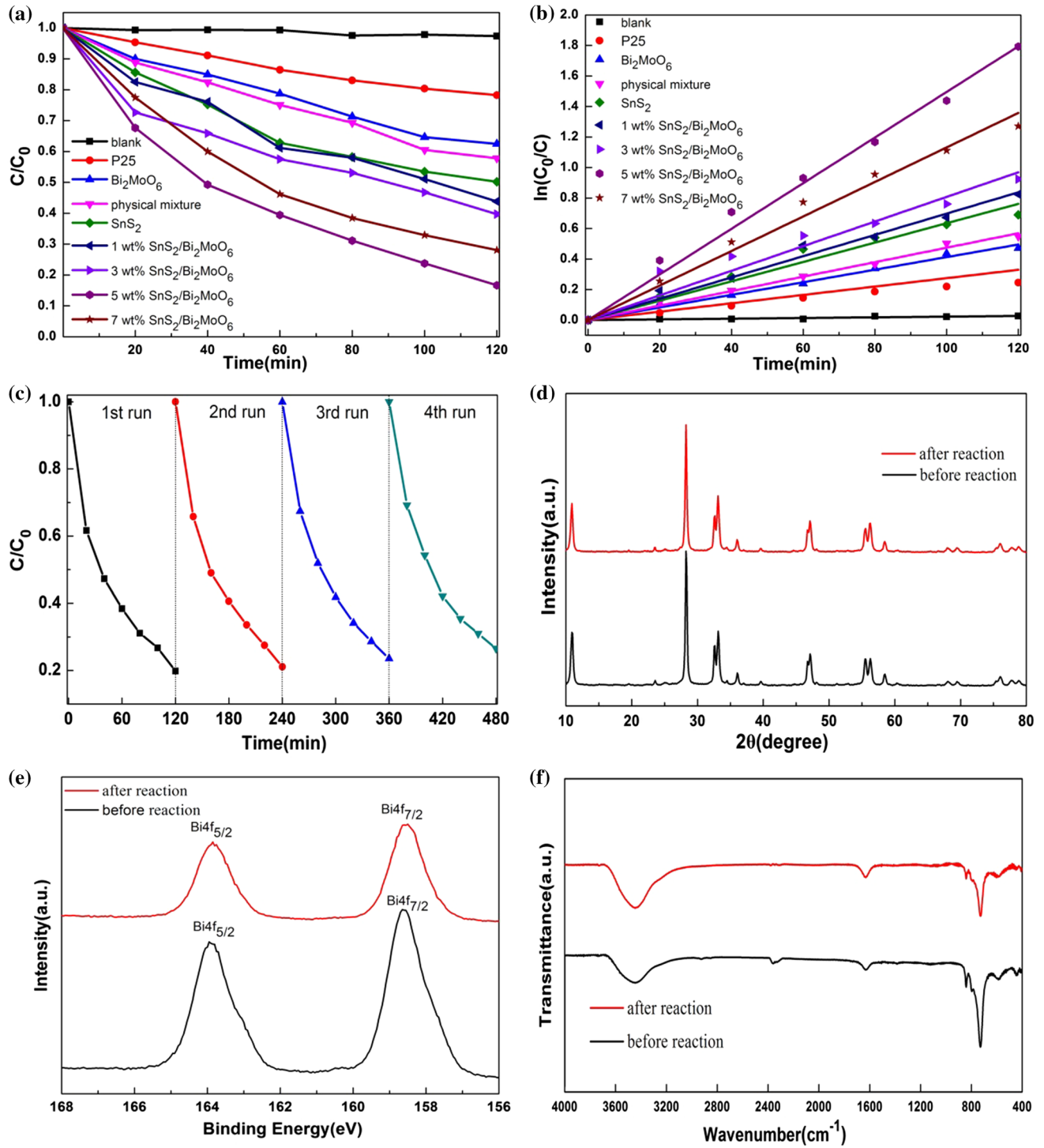
Figure 7 **a** Photocatalytic degradation of CV (20.0 mg L^{-1}). **b** The first-order kinetics of CV degradation with different samples. **c** Cycling runs for the photocatalytic degradation of CV with 5 wt% SnS_2/Bi_2MoO_6. **d** XRD patterns, **e** XPS spectra, and **f** FTIR spectra of 5 wt% SnS_2/Bi_2MoO_6 prior to and following the recovery test.

SnS_2, and 5 wt% SnS_2/Bi_2MoO_6 under white light irradiation, with the results displayed in Fig. 8. It may be seen that the CIP was degraded by 90% within 120 min. using the 5 wt% SnS_2/Bi_2MoO_6 catalyst, which was far more efficient than that when using pure SnS_2 or Bi_2MoO_6.

Table 2 Degradation rates and kinetic constants of the as-prepared samples

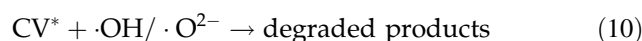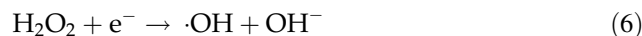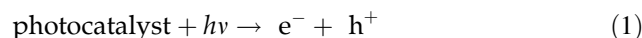| Sample	Degradation rate (%)	Rate constants (min^{-1})
Blank	3.0	0.0002
P25	22	0.0027
Bi_2MoO_6	38	0.0041
Physical mixture	42	0.0047
SnS_2	50	0.0064
1 wt% SnS_2/Bi_2MoO_6	57	0.0070
3 wt% SnS_2/Bi_2MoO_6	60	0.0081
5 wt% SnS_2/Bi_2MoO_6	84	0.0150
7 wt% SnS_2/Bi_2MoO_6	72	0.0113
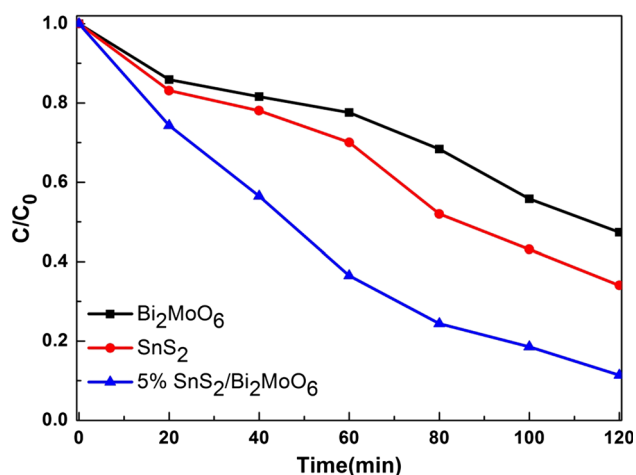
Figure 8 The photodegradation of CIP (10 mg L^{-1}) over pure Bi_2MoO_6, SnS_2, and 5 wt% SnS_2/Bi_2MoO_6.

Radical trapping experiments and ESR analysis

Trapping experiments were conducted to explore the photocatalytic mechanisms of SnS_2/Bi_2MoO_6. Three active species scavengers, benzoquinone (BQ), ethylenediamine tetraacetic acid disodium salt (EDTA-2Na), and isopropyl alcohol (IPA), were added into the photocatalytic CV degradation system to trap superoxide radicals ($\cdot O^{2-}$), holes (h^+), and hydroxyl radicals ($\cdot OH$), respectively, with the results shown in Fig. 9a. With the addition of EDTA-2Na and IPA, the photodegradation rates of the CV were significantly decreased, showing that h^+ and $\cdot OH$ radicals played important roles in the degradation process. In the same way, it could be concluded that $\cdot O^{2-}$ played a supportive role. In other words, it could be concluded that a $h^+ > \cdot OH > \cdot O^{2-}$ mechanism occurred during the photodegradation process.

On the basis of the trapping experiment results above, an ESR spectrometer (with DMPO) was implemented to detect h^+, $\cdot OH$, and $\cdot O^{2-}$ on the surface of the catalysts under white light irradiation [39]. As shown in Fig. 9b, strong DMPO h^+ species peaks could be observed over the 5 wt% SnS_2/Bi_2MoO_6 under dark conditions. In Fig. 9c and d, no ESR signal was found under dark conditions. With white light irradiation, four characteristic peaks of DMPO $\cdot OH$ and DMPO $\cdot O^{2-}$ were observed with an intensity ratio of 1:2:2:1 and 1:1:1:1, where the intensities of the $\cdot OH$ and $\cdot O^{2-}$ signals gradually increased in conjunction with longer irradiation times. Nevertheless, the peak intensities of DMPO h^+ and $\cdot OH$ increased more obviously compared with that of DMPO $\cdot O^{2-}$ in this system, which signified the critical roles of h^+ and $\cdot OH$ for the removal of CV, which were consistent with the experimental trapping results.

Based on the radical trapping experiments and ESR analysis results, the degradation process can be expressed as follows:
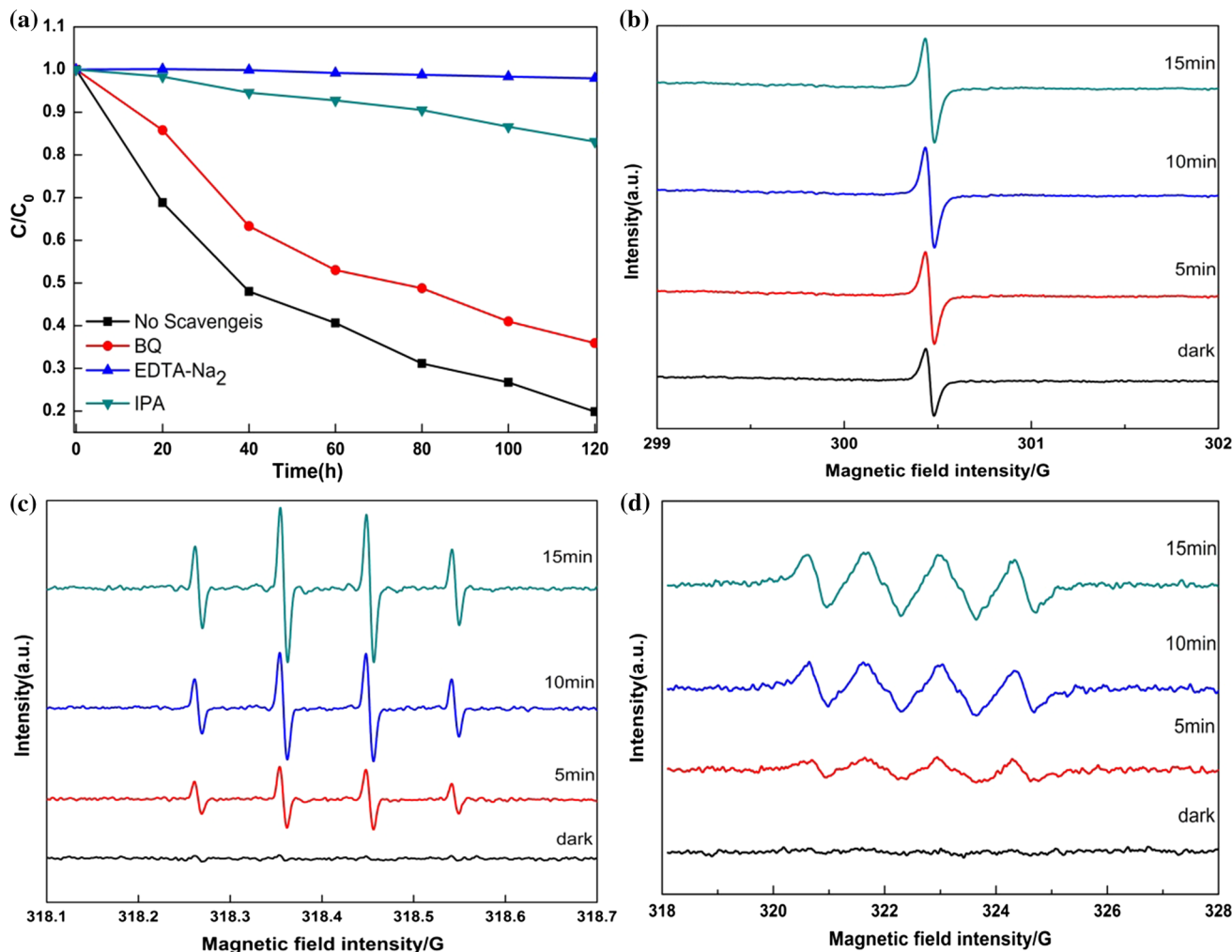
$$\text{photocatalyst} + hv \rightarrow \text{e}^- + \text{h}^+ \tag{1}$$

$$\text{CV} + hv \rightarrow \text{CV}^* + \text{e}^- \tag{2}$$

$$\text{O}_2 + \text{e}^- \rightarrow \cdot \text{O}^{2-} \tag{3}$$

$$\text{H}_2\text{O} + \cdot \text{O}^{2-} \rightarrow \cdot \text{HO}_2 + \text{OH}^- \tag{4}$$

$$2 \cdot \text{HO}_2 \rightarrow \text{H}_2\text{O}_2 + \text{O}_2 \tag{5}$$

$$\text{H}_2\text{O}_2 + \text{e}^- \rightarrow \cdot \text{OH} + \text{OH}^- \tag{6}$$

$$\text{H}_2\text{O} + \text{h}^+ \rightarrow \cdot \text{OH} + \text{H}^+ \tag{7}$$

$$\text{OH}^- + \text{h}^+ \rightarrow \cdot \text{OH} \tag{8}$$

$$\text{h}^+ + \text{CV} \rightarrow \text{CV}^* \tag{9}$$

$$\text{CV}^* + \cdot \text{OH}/ \cdot \text{O}^{2-} \rightarrow \text{degraded products} \tag{10}$$

Figure 9 Photocatalytic degradation curves of CV (20 mg L^{-1}) over 5 wt% SnS$_2$/Bi$_2$MoO$_6$ in the presence of different scavengers (**a**). ESR spectra of DMPO h$^+$ (**b**), DMPO ·OH (**c**) and DMPO ·O^{2-} (**d**) over 5 wt% SnS$_2$/Bi$_2$MoO$_6$ nanocomposite.

UV–vis diffuses reflectance spectra (DRS) analysis

The UV–vis DRS spectra in Fig. 10 revealed the optical absorption properties of the SnS$_2$, Bi$_2$MoO$_6$, and composites. As shown in Fig. 10a, the SnS$_2$/Bi$_2$MoO$_6$ composites exhibited excellent visible light absorption, and the absorption capacity of Bi$_2$MoO$_6$ was significantly enhanced with SnS$_2$ loading. The band gap of pure SnS$_2$ was calculated to be ∼ 2.23 eV, which corresponded to an absorption edge at 600 nm, whereas the band gap of pure Bi$_2$MoO$_6$ was ∼ 2.80 eV. Nevertheless, the 5 wt% SnS$_2$/Bi$_2$MoO$_6$ composites demonstrated a relatively narrow band gap of ∼ 2.40 eV, suggesting that the decoration of SnS$_2$ could broaden the photoresponse of Bi$_2$MoO$_6$ in the visible light range (Fig. 10b). The band edge positions of the Bi$_2$MoO$_6$ and SnS$_2$ could be evaluated by the empirical equations:

$$E_{VB} = X - E_0 + 0.5E_g \tag{11}$$

$$E_{CB} = E_{VB} - E_g \tag{12}$$

where X is the electronegativity of the semiconductor, and E_g is the band gap energy of the semiconductor. From the above analysis (Fig. 10b), it could be seen that the E_g of Bi$_2$MoO$_6$ and SnS$_2$ was 2.8 and 2.23 eV, respectively; E_0 is the energy of free electrons on the hydrogen scale (∼ 4.50 eV) [40]; E_{VB} is the valence band (VB) edge potential, and E_{CB} is the conduction band (VB) edge potential. The X values for Bi$_2$MoO$_6$ and SnS$_2$ were calculated to be 5.50 [41] and 4.66 eV [42], respectively. The calculation results revealed that the E_{VB} values of Bi$_2$MoO$_6$ and SnS$_2$ were 2.40 and 1.28 eV, whereas the E_{CB} values were

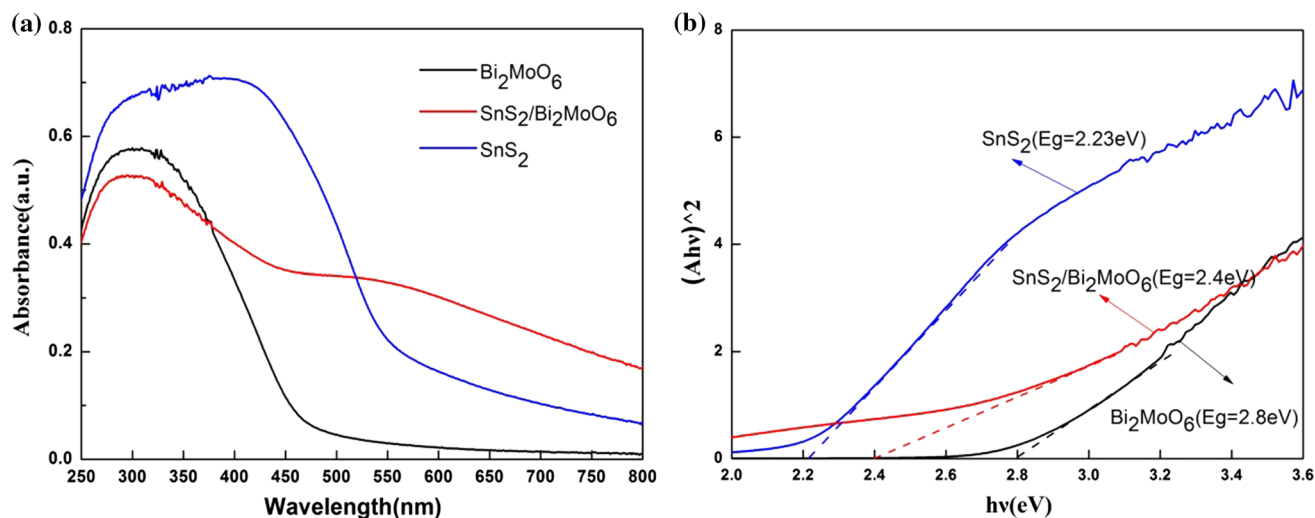**Figure 10** **a** UV–vis diffuse reflection spectra of Bi_2MoO_6, SnS_2, and 5 wt% SnS_2/Bi_2MoO_6 composites. **b** The curves of $(Ahv)^2$ versus hv for Bi_2MoO_6, SnS_2, and SnS_2/Bi_2MoO_6.

− 0.40 and − 0.95 eV, respectively. On the basis of the experimental results above, the potential mechanisms for the formation of SnS_2/Bi_2MoO_6 heterostructures were proposed and are illustrated in Fig. 11.

Potential photocatalytic mechanism

On the basis of the UV–vis DRS spectra and trapping detection results above, the potential mechanisms for the photocatalytic activity of the Z-scheme SnS_2/Bi_2MoO_6 system were proposed (Fig. 11) [43, 44], and the traditional electron-transfer mechanism could be expressed (Fig. 11a). The photoinduced electrons in the CB of the SnS_2 migrated to the

CB of the Bi_2MoO_6, while the photoinduced holes in the VB of the Bi_2MoO_6 migrated to the VB of the SnS_2 due to the more negative band potential of SnS_2. Nevertheless, the holes in the VB of SnS_2 could not react with H_2O or OH^- to generate ·OH, as the VB edge potential of SnS_2 was higher than the standard redox potential [45]; hence, it did not align with the trapping experiment results above. Thus, a potential mechanism of a direct Z-scheme was proposed (Fig. 11b). Both SnS_2 and Bi_2MoO_6 could be easily excited to yield electron–hole pairs under white light irradiation, and photogenerated electrons from the VB of the Bi_2MoO_6 transferred into the CB of the Bi_2MoO_6, which subsequently combined with the photogenerated holes of the SnS_2, and as a result, the

Figure 11 Proposed potential mechanism for the formation of SnS_2/Bi_2MoO_6 heterostructures.
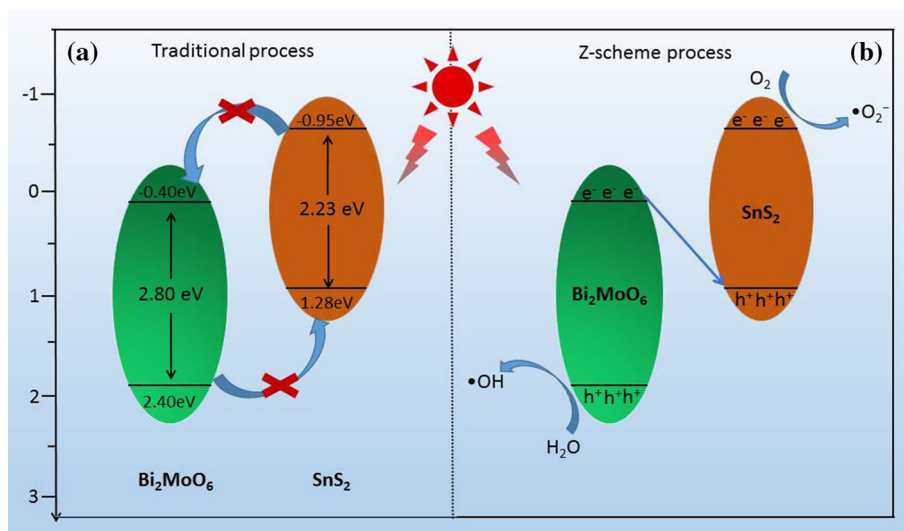
carriers were spatially separated. Therefore, the CB electrons of the SnS_2 could effectively reduce oxygen to form the reactive $\cdot O^{2-}$ species, which could further react with H^+ to produce $\cdot OH$, or initiate the direct oxidation of organic pollutants. On the other hand, the holes remaining in the VB of the Bi_2MoO_6 might be transferred to the surface of the photocatalyst, attack target organic compounds, or react with H_2O to form $\cdot OH$ [46]. Thus, the Z-scheme system could efficiently separate the photoinduced electron–hole pairs, to obtain enhanced photocatalytic performance for SnS_2/Bi_2MoO_6.

Conclusions

In summary, Z-scheme SnS_2/Bi_2MoO_6 photocatalysts were successfully synthesized through a facile hydrothermal method. Model CV and CIP pollutants were effectively degraded over SnS_2/Bi_2MoO_6 composites under white light irradiation. Further, the SnS_2/Bi_2MoO_6 composite exhibited high stability during cycling experiments. Radical trapping experiments and ESR results revealed that holes and $\cdot OH$ comprised the primary active species that were essential for the degradation of pollutants during the photocatalytic process. Furthermore, a photocatalytic Z-scheme mechanism was proposed to elucidate the improvement in photocatalytic efficiency. We trust that this work may provide further knowledge toward the design and synthesis of advanced photocatalysts, as well as to inspire further applications of photocatalysts for water purification under visible light irradiation.

Acknowledgements

References

[1] Fakhri A, Nejad PA (2016) Antimicrobial, antioxidant and cytotoxic effect of Molybdenum trioxide nanoparticles and application of this for degradation of ketamine under different light illumination. J Phys Chem B 159:211–217

[2] Fakhri A, Behrouz S (2015) Photocatalytic properties of tungsten trioxide (WO_3) nanoparticles for degradation of Lidocaine under visible and sunlight irradiation. Sol Energy 112:163–168

[3] Mohammadi S, Sohrabi M, Golikand A, Fakhri A (2016) Preparation and characterization of zinc and copper co-doped WO_3 nanoparticles: application in photocatalysis and photobiology. J Phys Chem B 161:217–221

[4] Fakhri A, Azad M, Tahami S (2017) Degradation of toxin via ultraviolet and sunlight photocatalysis using ZnO quantum dots/CuO nanosheets composites: preparation and characterization studies. J Mater Sci Mater Electron 28:16397–16402

[5] Fujishima A, Honda K (1972) Electrochemical photolysis of water at a semiconductor electrode. Nature 238:37–38

[6] Likodimos V, Chrysi A, Calamiotou M, Fernández-Rodrıguez C, Dona-Rodríguez JM, Dionysiouc DD, Falaras P (2016) Microstructure and charge trapping assessment in highly reactive mixed phase TiO_2 photocatalysts. Appl Catal B Environ 192:242–252

[7] Ayekoe PY, Robert D, Goné DL (2015) TiO_2/Bi_2O_3 photocatalysts for elimination of water contaminants. Part 1: synthesis of α-and β-Bi_2O_3 nanoparticles. Environ Chem Lett 13:327–332

[8] Dutta DP, Roy M, Tyagi AK (2012) Dual function of rare earth doped nano Bi_2O_3: white light emission and photocatalytic properties. Dalton Trans 41:10238–10248

[9] An HZ, Du Y, Wang TM, Wang C, Hao WC, Zhang JY (2008) Photocatalytic properties of BIOX (X = Cl, Br, and I). Rare Met 27:243–250

[10] Long MC, Cai WM, Cai J, Zhou BX, Chai XY, Wu YH (2006) Efficient photocatalytic degradation of phenol over $Co_3O_4/BiVO_4$ composite under visible light irradiation. J Phys Chem B 110:20211–20216

[11] Fulekar MH, Singh A, Dutta DP, Roy M, Ballald A, Tyagi AK (2014) Ag incorporated nano $BiPO_4$: sonochemical synthesis, characterization and improved visible light photocatalytic properties. Rsc Adv 4:10097–10107

[12] Dutta DP, Mandal BP, Naik R, Lawes G, Tyagi AK (2013) Magnetic, ferroelectric, and magnetocapacitive properties of sonochemically synthesized Sc-doped $BiFeO_3$ nanoparticles. J Phys Chem 117:2382–2389

[13] Zhang JL, Ma Z (2017) Flower-like Ag$_2$MoO$_4$/Bi$_2$MoO$_6$ heterojunctions with enhanced photocatalytic activity under visible light irradiation. J Taiwan Inst Chem Eng 71:156–164

[14] Xu YS, Zhang WD (2013) Anion exchange strategy for construction of sesame-biscuit-like Bi$_2$O$_2$CO$_3$/Bi$_2$MoO$_6$ nanocomposites with enhanced photocatalytic activity. Appl Catal B Environ 140:306–316

[15] Fakhri A, Rashidi S, Tyagi I, Agarwal S, Gupta V (2016) Photodegradation of Erythromycin antibiotic by γ-Fe$_2$O$_3$/SiO$_2$ nanocomposite: response surface methodology modeling and optimization. J Mol Liq 214:378–383

[16] Venugopal K, Rather HA, Rajagopal K, Shanthi MP, Sheriff K, Illiyas M, Rather RA, Manikandan E, Uvarajan S, Bhaskar M, Maaza M (2017) Synthesis of silver nanoparticles (Ag NPs) for anticancer activities (MCF 7 breast and A549 lung cell lines) of the crude extract of Syzygium aromaticum. J Phys Chem B 167:282–289

[17] Sun MH, Yin YY, Song CW, Wang YG, Xiao JK, Qu SC, Zheng WB, Li C, Dong W, Zhang L (2016) Preparation of Bi$_2$MoO$_6$ nanomaterials and theirs gas-sensing properties. J Inorg Organomet Polym 26:294–301

[18] Dutta DP, Ballal A, Chopade S, Kumar A (2017) A study on the effect of transition metal (Ti^{4+}, Mn^{2+}, Cu^{2+} and Zn^{2+})-doping on visible light photocatalytic activity of Bi$_2$MoO$_6$ nanorods. J Photochem Photobiol A 346:105–112

[19] Yu CL, Wu Z, Liu RY, Dionysiou DD, Yang K, Wang CY, Liu H (2017) Novel fluorinated Bi$_2$MoO$_6$ nanocrystals for efficient photocatalytic removal of water organic pollutants under different light source illumination. Appl Catal B Environ 209:1–11

[20] Lv JL, Dai K, Zhang JF, Geng L, Liang CH, Liu QC, Zhu GP, Chen C (2015) Facile synthesis of Z-scheme graphitic-C$_3$N$_4$/Bi$_2$MoO$_6$ nanocomposite for enhanced visible photocatalytic properties. Appl Surf Sci 358:377–384

[21] Li SJ, Hu SW, Zhang JL, Jiang W, Liu JS (2017) Facile synthesis of Fe$_2$O$_3$ nanoparticles anchored on Bi$_2$MoO$_6$ microflowers with improved visible light photocatalytic activity. J Colloid Interface Sci 497:93–101

[22] Ke J, Duan XG, Luo S, Zhang HY, Sun HQ, Liu J, Tade M, Wang SB (2017) UV-assisted construction of 3D hierarchical rGO/Bi$_2$MoO$_6$ composites for enhanced photocatalytic water oxidation. Chem Eng J 313:1447–1453

[23] Xu YS, Zhang WD (2013) Anion exchange strategy for construction of sesame-biscuit-like Bi$_2$O$_2$CO$_3$/Bi$_2$MoO$_6$ nanocomposites with enhanced photocatalytic activity. Appl Catal B Environ 140:306–316

[24] Yue D, Chen DM, Wang ZH, Ding H, Zong RL, Zhu YF (2014) Enhancement of visible photocatalytic performances of a Bi$_2$MoO$_6$–BiOCl nanocomposite with plate-on-plate

[25] heterojunction structure. Phys Chem Chem Phys 16:26314–26321

[25] Fakhri A, Behrouz S (2015) Assessment of SnS$_2$ nanoparticles properties for photocatalytic and antibacterial applications. Sol Energy 117:187–191

[26] Fakhri A, Kahi DS (2017) Synthesis and characterization of MnS$_2$/reduced graphene oxide nanohybrids for with photocatalytic and antibacterial activity. J Photochem Photobiol B 166:259–263

[27] Fakhri A, Behrouz S, Pourmand M (2015) Synthesis, photocatalytic and antimicrobial properties of SnO$_2$, SnS$_2$ and SnO$_2$/SnS$_2$ nanostructure. J Photochem Photobiol B 149:45–50

[28] Fakhri A, Khakpour R (2015) Synthesis and characterization of carbon or/and boron-doped CdS nanoparticles and investigation of optical and photoluminescence properties. J Lumin 160:233–237

[29] Fakhri A, Naji M, Fatolahi L, Nejad PA (2017) Synthesis and characterization of Fe$_3$O$_4$ and CdTe quantum dots anchored SnO$_2$ nanofibers and SnO$_2$ nanospheres for degradation and removal of two carcinogen substance. J Mater Sci Mater Electron 28:16484–16492

[30] Luo J, Zhou XS, Ma LM, Xu XY, Du ZH, Zhang JQ (2016) Enhancing visible light photocatalytic activity of direct Z-scheme SnS$_2$/Ag$_3$PO$_4$ heterojunction photocatalysts. Mater Res Bull 81:16–26

[31] Di TM, Zhu BC, Cheng B, Yu JG, Xu JS (2017) A direct Z-scheme g-C$_3$N$_4$/SnS$_2$ photocatalyst with superior visible-light CO$_2$ reduction performance. J Catal 352:532–541

[32] Li HP, Deng QH, Liu JY, Hou WG, Du N, Zhang RJ, Tao XT (2014) Synthesis, characterization and enhanced visible light photocatalytic activity of Bi$_2$MoO$_6$/Zn–Al layered double hydroxide hierarchical heterostructures. Catal Sci Technol 4:1028–1037

[33] Miao YC, Yin HB, Peng L, Huo YN, Li HX (2016) BiOBr/Bi$_2$MoO$_6$ composite in flower-like microspheres with enhanced photocatalytic activity under visible-light irradiation. RSC Adv 6:13498–13504

[34] Li HP, Liu JY, Hou WG, Du N, Zhang RJ, Tao XT (2014) Synthesis and characterization of gC$_3$N$_4$/Bi$_2$MoO$_6$ heterojunctions with enhanced visible light photocatalytic activity. Appl Catal B Environ 160:89–97

[35] Zhang MY, Shao CL, Zhang P, Su CY, Zhang X, Liang PP, Sun YY, Liu YC (2012) Bi$_2$MoO$_6$ microtubes: controlled fabrication by using electrospun polyacrylonitrile microfibers as template and their enhanced visible light photocatalytic activity. J Hazard Mater 225:155–163

[36] Liu YP, Chen P, Chen Y, Lu HD, Wang JX, Yang ZS, Lu ZH, Li M, Fang L (2016) In situ ion-exchange synthesis of SnS$_2$/

g-C$_3$N$_4$ nanosheets heterojunction for enhancing photocatalytic activity. RSC Adv 6:10802–10809

[37] Khélia C, Boubaker K, Nasrallah TB, Amlouk M, Belgacem S (2009) Morphological and thermal properties of β-SnS$_2$ sprayed thin films using Boubaker polynomials expansion. J Alloys Compd 477:461–467

[38] Vasconcelos TG, Kümmerer K, Henriques DM, Martins AF (2009) Ciprofloxacin in hospital effluent: degradation by ozone and photoprocesses. J Hazard Mater 169:1154–1158

[39] Zhao W, Ma WH, Chen CC, Zhao JC, Shuai ZG (2004) Efficient degradation of toxic organic pollutants with Ni$_2$O$_3$/TiO$_{2-x}$B$_x$ under visible irradiation. J Am Chem Soc 126:4782–4783

[40] Xu YS, Yu YX, Zhang WD (2014) Wide bandgap Bi$_2$O$_2$.CO$_3$-coupled Bi$_2$MoO$_6$ heterostructured hollow microspheres: one-pot synthesis and enhanced visible-light photocatalytic activity. J Nanosci Nanotechnol 14:6800–6808

[41] Zhang J, Niu CG, Ke J, Zhou LF, Zeng GM (2015) Ag/AgCl/Bi$_2$MoO$_6$ composite nanosheets: a plasmonic Z-scheme visible light photocatalyst. Catal Commun 59:30–34

[42] Zhang JL, Zhang LS, Yu N, Xu KB, Li SJ, Wang HL, Liu JS (2015) Flower-like Bi$_2$S$_3$/Bi$_2$MoO$_6$ heterojunction superstructures with enhanced visible-light-driven photocatalytic activity. RSC Adv 5:75081–75088

[43] Hiroaki T, Tomohiro M, Tomokazu K, Tomoki A, Koji T (2006) All-solid-state Z-scheme in CdS–Au–TiO$_2$ three-component nanojunction system. Nat Mater 5:782–786

[44] Katsumata H, Sakai T, Suzuki T, Kaneco S (2014) Highly efficient photocatalytic activity of g-C$_3$N$_4$/Ag$_3$PO$_4$ hybrid photocatalysts through Z-scheme photocatalytic mechanism under visible light. Ind Eng Chem Res 53:8018–8025

[45] Zhang WP, Xiao XY, Zeng XY, Li Y, Zheng LL, Wan CX (2016) Enhanced photocatalytic activity of TiO$_2$ nanoparticles using SnS$_2$/RGO hybrid as co-catalyst: DFT study and photocatalytic mechanism. J Alloys Compd 685:774–783

[46] Hao YC, Dong XL, Zhai SR, Wang XY, Ma HC, Zhang XF (2016) Towards understanding the photocatalytic activity enhancement of ordered mesoporous Bi$_2$MoO$_6$ crystals prepared via a novel vacuum-assisted nanocasting method. RSC Adv 6:35709–35718